



Interpretation of gravity and magnetic data on the hot dry rocks (HDR) delineation for the enhanced geothermal system (EGS) in Gonghe town, China

Xueyu Zhao^{1,2} · Zhaofa Zeng¹ · Yangang Wu¹ · Rongqin He¹ · Qiong Wu¹ · Senqi Zhang³

Received: 29 May 2019 / Accepted: 10 August 2020 / Published online: 16 August 2020
© Springer-Verlag GmbH Germany, part of Springer Nature 2020

Abstract

As a new kind of renewable and environmental-friendly energy to generate electricity, hot dry rocks (HDR) geothermal reservoirs have been studied, along with the enhanced geothermal system (EGS). Geophysical methods have been used for the geological characterisation in different scales. The small-scale geophysical data are required for the local geological analysis so as to provide prior information for HDR modelling. Gonghe basin is in the northeast margin of the Qinghai–Tibet Plateau. Several drilling records indicate that this basin is a potential HDR prospecting area with high geothermal gradient, high heat flow and widespread igneous rock distribution, especially the Gonghe town (Qiabuqia) along with its neighbouring area. Gravity and magnetic surveys were carried out here. To better understand the areal and vertical distribution of the HDR, the gravity and magnetic data were inverted using 2D manual inversion and 3D cross-gradient joint inversion based on the smooth l^0 norm constraint of minimum support functional stabiliser. The 2D model showed the sedimentary cap with a thickness of around 1000–1500 m. Granites of different periods and intrusion process were widely distributed and underlined the sediments accompanied by some deep faults. As for the HDR delineation, 3D models showed a potential area along Gonghe town and Dongba. The density and susceptibility were estimated at over 2.6 g/cm^3 and 4×10^{-3} SI separately, when referred with exiting HDR distribution along the geological profile of DR4–QR1–DR3–DR2 wells. The upper boundary of HDR was outlined at the depth of around 2000 m, and the volume of HDR was then estimated around 6100 km^3 above 3500 m depth. The appearance of the density and susceptibility models was affected by the lithology, stress and hydrothermal alteration. More precise geophysical methods including the microgravity, seismic and MT (magnetotelluric) surveys would be more applicable at the HDR exploitation stage.

Keywords Hot dry rocks (HDR) · Enhanced geothermal system (EGS) · Gravity and magnetic data · 2D manual modelling · 3D joint inversion · Gonghe area

Introduction

Hot dry rock (HDR) is a new kind of renewable and environmental-friendly energy to be exploited for electricity generation (Zarrouk and Moon 2014). Typically, this geothermal energy is often stored in high temperature and low permeable crystalline rocks at a depth of at least 2000 m with an in situ temperature typically above $150 \text{ }^\circ\text{C}$ (Maxwell 2014). The enhanced geothermal system (EGS) is commonly used for petrothermal systems if their permeability is artificially increased due to hydraulic stimulation. To extract the heat from HDR, EGS is also applied with artificial water injection due to the low and no permeability of HDR reservoir. This system involves a dual-well system by pumping cold fluids through a well into HDR, then extracting the heated fluids

✉ Xueyu Zhao
xueyu.zhao@student.unsw.edu.au

✉ Zhaofa Zeng
zengzf@jlu.edu.cn

¹ College of Geoexploration Science and Technology, Jilin University, Changchun 130026, China

² School of Biological, Earth and Environmental Sciences, UNSW Australia, Kensington, NSW 2052, Australia

³ Center for Hydrogeology and Environmental Geology, China Geological Survey, Baoding 071051, China

through another well (Jelacic et al. 2008). Many EGS projects have been tested in the USA, UK, Japan, Germany and Australia, while there is no successful commercial plant due to the high cost of system development (Panel 2006; Chen and Jiang 2015; Xie and Min 2016). In China, the study of HDR started in 2010 (Lu et al. 2017). It has been estimated that the total HDR energy in China is 20.9×10^6 EJ, which is equivalent to the standard coal of 714.9×10^{12} t (Wang et al. 2012). Gonghe basin, Songliao basin and Yangbajiang have been selected as the potential areas for further HDR study (Guiling et al. 2020).

As tools for geothermal resource exploration, geophysical methods are often applied for geological analysis and modelling in geothermal fields. When considering the density and susceptibility contrast, gravity and magnetic data are applied for delineating the geological structure, such as buried faults, the depth of Moho interface and the Curie point depth (e.g. Uwiduhaye et al. 2018; Xi et al. 2018; Zaher et al. 2018; Zhao et al. 2019). The electromagnetic (EM) methods [e.g. MT (magnetotelluric)] could also delineate the faults and potential geothermal areas. The high conductivity or low resistivity anomalies could reflect the distribution of hot-saline fluids, resistive host rocks, or even partial melting (Peacock et al. 2012; Kana et al. 2015; Samrock et al. 2015). At the exploitation stage, the seismic method (e.g. the P-wave or S-wave analyse) could also be used for the faults and granite mapping, as well as the fracture monitoring (Khair et al. 2015; Li et al. 2018; Fan et al. 2020).

The Gonghe geothermal field is in the north-eastern margin of the Qinghai–Tibet Plateau. Several works on the geothermic mechanism were conducted in this area. Zhao et al. (2020) outlined the possible buried faults and calculated the regional depth of Moho interface and Curie point depth by large-scale gravity and magnetic data, with the assumption of the heat source in the upper crust. Gao et al. (2018) used 3D MT imaging method to characterise 3D resistivity models with the conclusion of heat source at the middle crust in the Gonghe Basin. Furthermore, Zhang et al. (2018a) measured the latest heat flow and conducted the 1D theoretical crustal thermal structures simulation. The unusual heat flow here was caused by the cooling of a shallow magma chamber. For the theoretical study, Xu et al. (2018) simulated the power generation potentiality for EGS and provided the strategy for the HDR exploitation, along the profile of DR4–QR1–DR3–DR2 wells in Qiabuqia (Gonghe town).

Current geophysical studies in this area are mainly focused on the regional structure. Small-scale geophysical data are thereby required for the local geological analysis so as to provide prior information for the EGS site determination and HDR modelling. In this paper, we aim to use gravity and magnetic data in Gonghe town and its surrounding area to conduct the density and susceptibility modelling. 2D manual inversion was conducted for the analysis of the

geological structure, in-depth to 10 km. 3D joint inversion shows the models within 3500 m depth. With lithology record and temperature log along DR4–QR1–DR3–DR2 wells, the HDR distribution and application for energy production was then described.

Regional setting

Gonghe basin is in the middle-west part of China and the northeast margin of the Qinghai–Tibet Plateau. In this area, the topography is majorly dominated by the Qinghai–Tibet Plateau (Sun et al. 2007). Many hydrothermal springs have been discovered along the NE–SW and N–S extending faults (Liu et al. 2017) and the hot water comes from the deeper part of the basin (~1000 m), with a high concentration of arsenic and other minerals (Fang et al. 2009). Thermal survey results also reveal an excellent geothermal condition in this basin, in terms of geothermal gradient and terrestrial heat flow. The geothermal gradient could be over 6.8 °C/100 m, and the temperature at a depth of 3705 m could be 236 °C (Yue et al. 2015; Zhang et al. 2018b). The heat flow here is as high as 119.3 mW/m² (Xu et al. 2019), far more than the world's mean rate (65 mW/m² over continental crust) (Pollack et al. 1993).

This basin is also named as the Gonghe Aulacogen (Zhang et al. 2004), with a complex geological background (e.g. He et al. 2017). Generally, it is tectonically controlled by the sinistral strike-slip framework of the Kunlun Orogen, Qinling Orogen to the south and Qilian Orogen to the north in Fig. 1a (Fang et al. 2005). The edges are surrounded by several faults, which formed in the Cenozoic era accompanying volcanic eruptions. For different directions, it is bordered by the foothills of the Qinghainan Fault (north), the Animaqing Suture Zone (extended from Kunlun Fault) (south), the Wahongshan Fault (West) and the Duohehao Fault (east). Besides, the Yellow River flows in the central part of the basin and spills this basin with an NE orientation. These NNW–SSE and NWW–SEE faults bounding the basin give rise to its rhomboid shape (Zhang et al. 2006).

Quaternary and Neogene sediments mainly cover the land in this area. The Cenozoic overburden thickness in this basin could be greater than 5000 m (Sun et al. 2011). Near the Gonghe town, the thickness of the sedimentary layers is around 1300–1500 m, where the hot water mainly originates. Moreover, the main igneous rocks, including granite and granodiorite, are more widely distributed (Zhang et al. 2006). The granite rocks were formed in Indosinian and Yanshanian periods and laid the basement at a depth of over 2000 m. The granite with temperatures more than 150 °C is the main target of the HDR reservoir (Yan 2015; Zhang et al. 2018b).

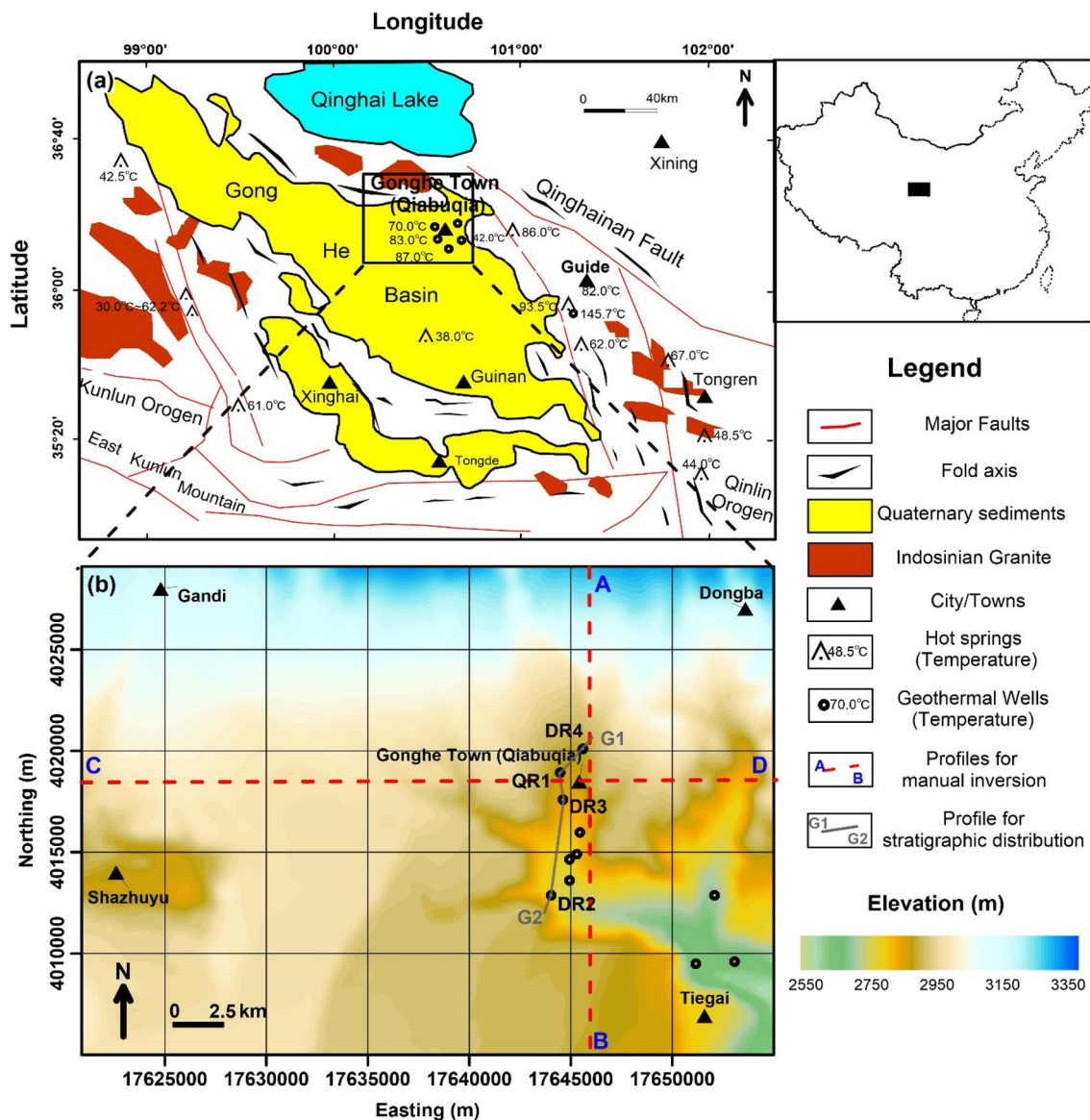


Fig. 1 a Simplified tectonic map of Gonghe–Guide area and its neighbouring region (after Zhang et al. 2018) including the location of the study area. (b) Topographic map of the study area. AB and CD

indicate the position of the manual inversion profiles. G1–G2 indicates the position of stratigraphic distribution profile in Fig. 5

Materials and methods

Study area

Our study area is the Gonghe town (Qiabuqia) with its surrounding area. It is in the north-central part of the Gonghe Basin and located about 30 km south away from the Qinghai Lake. It covers approximately 820 km² (Fig. 1a), and the elevation ranges from 2550 to 3350 m above the sea level. It is higher in the north part, at the northing of 4025 000–4027 000 m. The lowest area is in the south-eastern part near the Tiegai town.

Prior to the gravity and magnetic measurements, more than ten wells have been drilled here (e.g. DR4, QR1, QR3, DR2 and GR1). The temperature could reach around 203 °C at 3600 m depth in the well GR1 (not shown in the figure) (Zhang et al. 2018b). The lithology drilling records also indicate a two-layer system here. That is, the shallow part is the hydrothermal reservoir, with the sediments of around 900–1500 m thickness. It is underlain by granite, which is the target HDR area (Xu et al. 2018). Besides, the thermal testing for granite samples here shows the average thermal conductivity of 1.86 W/(m K) and the heat generation rate of 2.41–5.73 μW/m³ (Zhang et al. 2018a).

Gravity and magnetic data collection and interpolation

For the data collection, we used the CG-5 relative gravimeter and GSM-19T proton precession magnetometer to gather the gravity and magnetic data, respectively (Reudink et al. 2014). GPS was used to acquire positioning coordinates at each station. In total, the gravity dataset consists of 4200 stations with a spacing of approximately 500 m. The magnetic dataset has 7360 stations with around 200 m spacing.

Raw gravity data were corrected through the standard corrections to achieve the complete Bouguer anomaly (Uwuhaye et al. 2018). Free air and Bouguer corrections were calculated using the International Association of Geodesy 1967 formula (Tóth et al. 2005) and terrain correction was applied with the 90 m-SRTM data (Jarvis et al. 2008). The original magnetic data were also corrected, including the normal correction and diurnal correction (Dobrin and Savit, 1960; Nabighian et al. 2005). Meanwhile, reduction to magnetic poles was also conducted, as magnetic anomalies usually do not overlap with the structure (Over et al. 2018). The processed gravity and magnetic (anomaly) data were then interpolated across the study area onto a common 200-m grid, using ordinary local kriging and a neighbourhood of 20–30 points.

Regional–residual separation of gravity and magnetic data

The Bouguer gravity anomaly and magnetic anomaly are controlled by a regional trend resulting from the presence of deep and large structures. In most cases, there is no information on density or magnetic susceptibility heterogeneities in the deep zones (Gabtni and Jallouli 2017). Many methods have been applied to the regional–residual separation, such as second and higher polynomial fitting and upward continuation (Jacobsen 1987; Wang 2006; Zeng et al. 2007; Represas et al. 2013).

In this paper, we used the upward continuation to filter the gravity and magnetic data. This method attenuates high wavelength anomalies related to shallow geological bodies and provides a possibility to image deeper structures associated with regional gravity and magnetic patterns. To extract a regional field at a depth of z_0 , the height of upward continuation as $2z_0$ is required (Gabtni and Jallouli 2017). In this way, the residual anomaly could be then regarded as the response from the shallow geological bodies. When it goes to the HDR delineation, the upper boundary has been achieved is around 2500 m (Xu et al. 2018). Therefore, we chose 7 km as the height of upward continuation, then the residual anomaly could then reflect the density and magnetic susceptibility distribution in those parts of the area which are shallower than 3500 m.

2D manual modelling

The principal application of the magnetic and gravity data is to determine the depth of the anomalous sources of the observed anomalies, and the quantitative interpretation of the gravity and magnetic could be carried out through trial-and-error modelling assuming the 2D approach. Oasis Montaj software is used in gravity and magnetic processing, interpretation and visualisation. In this software, we could conduct 2D modelling via a module called gym-sys. The initial geophysical model could be set up according to the MT or seismic evidence, and then we need to adjust the shape or value of the model so that the calculated curve fits the raw data curves as much as possible (Oasis Montaj 2006).

We selected two profiles AB and Cd across the study area (Fig. 1b). The profile AB was in the NS direction and passed near the wells and the Gonghe town. The profile CD was in the EW direction and across the town. Prior to manual modelling, the initial model creation was mandatory. We referred to the MT inversion models by Gao et al. (2018). His results revealed that the surface down to around 2000–3000 m was a conductive zone corresponding to the Quaternary and Neogene sediments. A high resistivity zone below this area was down to ~10 to 15 km depth, which was associated with non-weathered metamorphic and igneous rocks. Therefore, our initial model was then set up with three parts from the surface to the depth of around 12 km. The upper one was regarded as the Quaternary sediments, the middle one was Neogene sediments, and the bottom was the granite rocks. For the average density value, the Quaternary and Neogene sediments in Qinghai Province were measured as 1.80 and 2.34 g/cm³, respectively (Hu 1991). In the study area of Gonghe town, the experimental density and magnetic susceptibility of granites are 2.532–2.555 g/cm³ and $0.0456 \times 10^{-3} \sim 13.847 \times 10^{-3}$ SI separately (Xing 2017).

3D cross-gradient joint inversion

Unlike manual modelling, which needs labours to modify models, 3D inversion with optimisation algorithm could achieve the models automatically. Regarding the structural similarity, the rock structure or boundaries may coincide between different geophysical models (e.g. density, susceptibility), and thus the joint inversion could serve for multiple property coupling and integration (Gallardo and Meju 2011). The cross-gradient function could detect differences of physical property fields within large or small gradients without any discontinuities or singularities, so the cross-gradient joint inversion has also been applied and proven to be useful and stable, through various applications on multiple joint inversion problems (Pak et al. 2017). However, this kind of joint inversion relies on the algorithm of the single dataset inversion. In this paper, we used the gravity

and magnetic joint inversion based on the smooth l^0 norm constraint of minimum support functional stabiliser (SLO-MS) (Portniaguine and Zhdanov 2002; Zhang et al. 2020). It shows the ability to generate focused images for geological structures with higher efficiency.

For this method, the minimisation of the cross-gradient joint inversion is specified as (Gallardo and Meju 2004; Pak et al. 2017):

$$\min \varphi = \varphi_g + \varphi_{mag}, \text{ subject to } \tau = 0 \tag{1}$$

where φ stands for the objective function for the joint inversion, φ_g and φ_{mag} are the objective functions of single gravity or magnetic inversion, τ is the cross-gradient of the density and susceptibility model data sets.

φ_g and φ_{mag} are expressed as

$$\begin{aligned} \varphi_g = & (\mathbf{W}_{d_g} \mathbf{A}_g(\mathbf{m}_g) - \mathbf{W}_{d_g} \mathbf{d}_g)^T (\mathbf{W}_{d_g} \mathbf{A}_g(\mathbf{m}_g) - \mathbf{W}_{d_g} \mathbf{d}_g) \\ & + \alpha_g \left(\mathbf{W}_{e_g}^{SLO} \mathbf{W}_{m_g} \mathbf{m}_g - \mathbf{W}_{e_g}^{SLO} \mathbf{W}_{m_g} \mathbf{m}_{g\cdot apr} \right)^T \\ & \left(\mathbf{W}_{e_g}^{SLO} \mathbf{W}_{m_g} \mathbf{m}_g - \mathbf{W}_{e_g}^{SLO} \mathbf{W}_{m_g} \mathbf{m}_{g\cdot apr} \right). \end{aligned} \tag{2}$$

$$\begin{aligned} \varphi_{mag} = & (\mathbf{W}_{d_{mag}} \mathbf{A}_{mag}(\mathbf{m}_{mag}) - \mathbf{W}_{d_{mag}} \mathbf{d}_{mag})^T (\mathbf{W}_{d_{mag}} \mathbf{A}_{mag}(\mathbf{m}_{mag}) \\ & - \mathbf{W}_{d_{mag}} \mathbf{d}_{mag}) + \alpha_{mag} \left(\mathbf{W}_{e_{mag}}^{SLO} \mathbf{W}_{m_{mag}} \mathbf{m}_{mag} - \mathbf{W}_{e_{mag}}^{SLO} \mathbf{W}_{m_{mag}} \mathbf{m}_{mag\cdot apr} \right)^T \\ & \left(\mathbf{W}_{e_{mag}}^{SLO} \mathbf{W}_{m_{mag}} \mathbf{m}_{mag} - \mathbf{W}_{e_{mag}}^{SLO} \mathbf{W}_{m_{mag}} \mathbf{m}_{mag\cdot apr} \right). \end{aligned} \tag{3}$$

$$\tau(\mathbf{m}_g, \mathbf{m}_{mag}) = \nabla \mathbf{m}_g \times \nabla \mathbf{m}_{mag}. \tag{4}$$

For (2)–(4), the subscripts g, mag are related to the gravity (density) and magnetic (susceptibility), respectively. φ is the objective function, \mathbf{W}_d is the covariance matrix of the observed dataset, \mathbf{A} is the kernel for forward, \mathbf{m} is the model matrix, \mathbf{d} is the observed dataset, α is the damping factor, \mathbf{W}_e^{SLO} is the weighting matrix constrained by smooth l^0 norm method, \mathbf{W}_m is the covariance matrix of models, \mathbf{m}_{apr} is the prior model matrix, T stands for the transpose, ∇ is the gradient, τ is the cross-gradient of the density and susceptibility models.

Using first-order Taylor expansion:

$$\mathbf{t}(\sigma, \kappa) = \mathbf{t}(\sigma^0, \kappa^0) + [\mathbf{B}^g \ \mathbf{B}^m] \begin{bmatrix} \sigma - \sigma^0 \\ \kappa - \kappa^0 \end{bmatrix}. \tag{5}$$

σ, κ represent the density and susceptibility models, and $\mathbf{B}^g, \mathbf{B}^m$ are the corresponding cross-gradient partial derivative, that is, $\mathbf{B}^g = \frac{\partial \mathbf{t}(\sigma, \kappa)}{\partial \sigma}$ and $\mathbf{B}^m = \frac{\partial \mathbf{t}(\sigma, \kappa)}{\partial \kappa}$.

The variational form for that would be

$$\begin{aligned} \delta P_g^{\alpha_g}(\mathbf{m}_g^{\omega_g}, \mathbf{d}_g^{\omega_g}) = & 2 \left(\delta \mathbf{m}_{mag}^{\omega_{mag}} \right)^T \left(\mathbf{F}_{\omega_g}^T \left(\mathbf{A}_g^{\omega_g}(\mathbf{m}_g^{\omega_g}) - \mathbf{d}_g^{\omega_g} \right) \right. \\ & \left. + \alpha_g \left(\mathbf{m}_g^{\omega_g} - \mathbf{m}_{g\cdot apr}^{\omega_g} \right) + \mu_g \mathbf{B}_g^T \mathbf{t} \left(\mathbf{m}_g^{\omega_g}, \mathbf{m}_{mag}^{\omega_{mag}} \right) \right) \end{aligned} \tag{6}$$

$$\begin{aligned} \delta P_{mag}^{\alpha_{mag}}(\mathbf{m}_{mag}^{\omega_{mag}}, \mathbf{d}_{mag}^{\omega_{mag}}) = & 2 \left(\delta \mathbf{m}_{mag}^{\omega_{mag}} \right)^T \left(\mathbf{F}_{\omega_{mag}}^T \left(\mathbf{A}_{mag}^{\omega_{mag}}(\mathbf{m}_{mag}^{\omega_{mag}}) - \mathbf{d}_{mag}^{\omega_{mag}} \right) \right. \\ & \left. + \alpha_{mag} \left(\mathbf{m}_{mag}^{\omega_{mag}} - \mathbf{m}_{mag\cdot apr}^{\omega_{mag}} \right) + \mu_{mag} \mathbf{B}_{mag}^T \mathbf{t} \left(\mathbf{m}_g^{\omega_g}, \mathbf{m}_{mag}^{\omega_{mag}} \right) \right) \end{aligned} \tag{7}$$

In (6) and (7), $\mathbf{F}_{\omega_{type}} = \mathbf{W}_{d_{type}} \mathbf{F}_{type} \mathbf{W}_{m_{type}}^{-1} \left(\mathbf{W}_{e_{type}}^{SLO} \right)^{-1}$ with the corresponding type of gravity or magnetic methods. \mathbf{F}_{type} is the Fréchet partial derivative matrix of $\mathbf{A}_{type}(\mathbf{m}_{type})$.

With the optimisation algorithm, such as the conjugate gradient method, the density and susceptibility models would be achieved when it meets the maximum iteration times or the RMS requirement.

Results

Spatial distribution of gravity and magnetic data

For the original kriged data, the gravity anomaly value (Fig. 2a) ranges from -400 to -360 mGal. In the north and southeast edge, it is higher ($-380 \sim -365$ mGal), while the central part is dominated by a lower negative anomaly ($-395 \sim -400$ mGal). As for the magnetic anomaly in Fig. 2b, it has a different tendency with the range from -10 to 195 nT. The zone with high value ($50\text{--}90$ nT) is concentrated in the middle part with an NNE–SSW trend.

The regional gravity anomaly in Fig. 2c is similar to the original one but with a smoother trend. The value is in a low rate ($-395 \sim -387$ mGal) in the Gonghe and Shazhuyu towns. The regional magnetic anomaly shown in Fig. 2d also keeps a similar trend, and the edges are more apparent in the south part of Gonghe town.

The spatial distribution of residual anomalies in Fig. 2e, f appear differently from the original kriged and regional data. For the gravity result, the value is from -5.4 to -1.4 mGal. The whole area is majorly covered by the high anomaly (> -3.1 mGal), while it is lower in the west and southeast margins (< -4.0 mGal). The residual magnetic anomaly ranges in $-8 \sim 22$ nT. Similarly, there is still a low-value zone (< -3 nT) in the north-eastern part of Gonghe town. However, the remaining area is in a medium value ($-2 \sim 6$ nT).

2D manual inversion modelling

Figure 3 shows the 2D manual joint inversion models of gravity and magnetic data in AB and CD profiles. For these two models, the geophysical responses match the observed data well, as the RMS is 3.246 (magnetic in AB), 0.79 (gravity in AB), 1.551 (magnetic in CD), 1.99 (gravity in CD). In AB profile, the magnetic curve fluctuates, and it is higher in the northern part. In contrast, the gravity curve goes down and then up smoothly. In CD, the magnetic value also

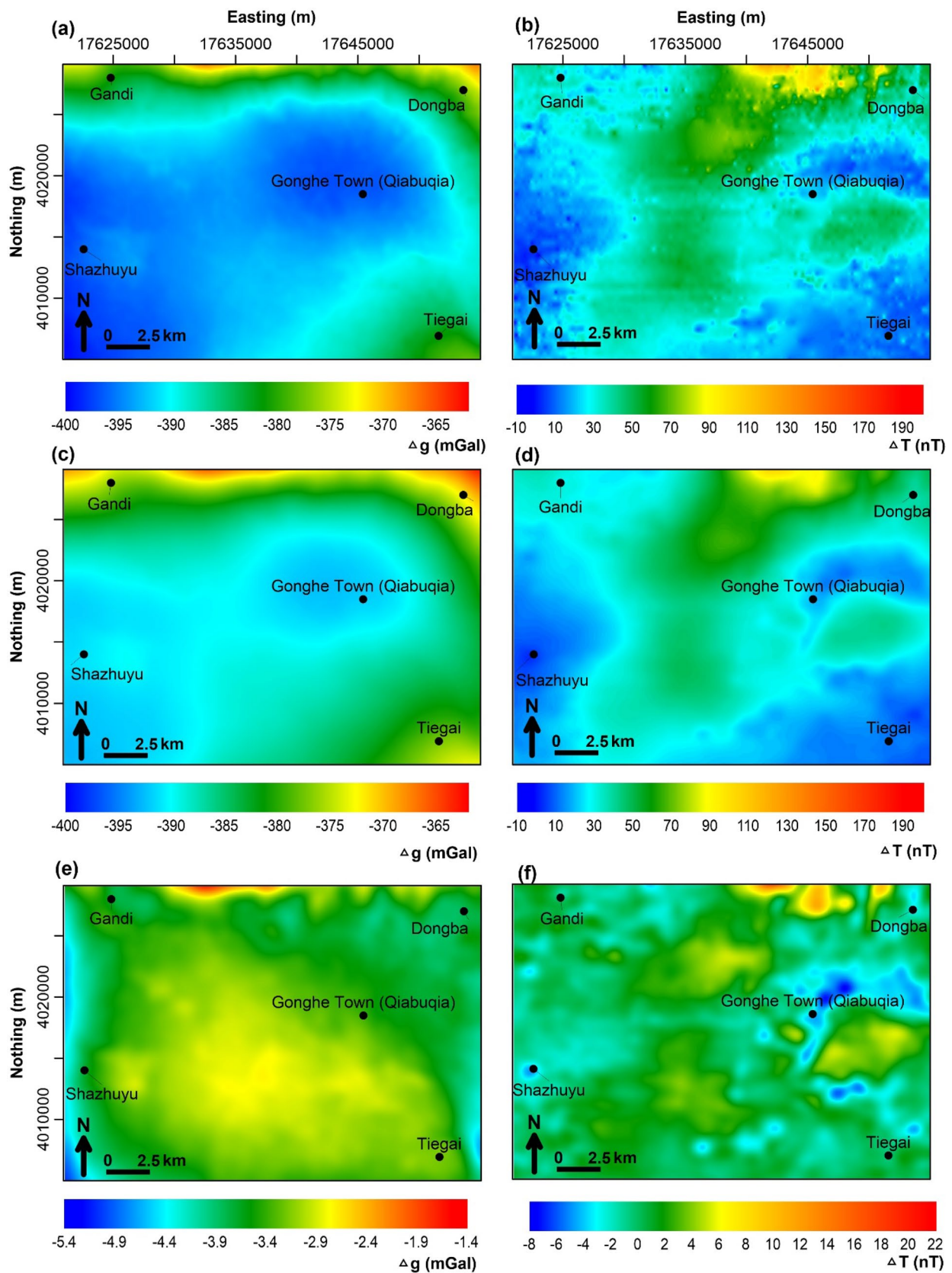


Fig. 2 Spatial distribution in the study area of (a) gravity kriged data; (b) magnetic kriged data. Through the upward continuation with the height of 7 km: (c) gravity regional data, (d) magnetic regional data, (e) gravity residual data and (f) magnetic residual data

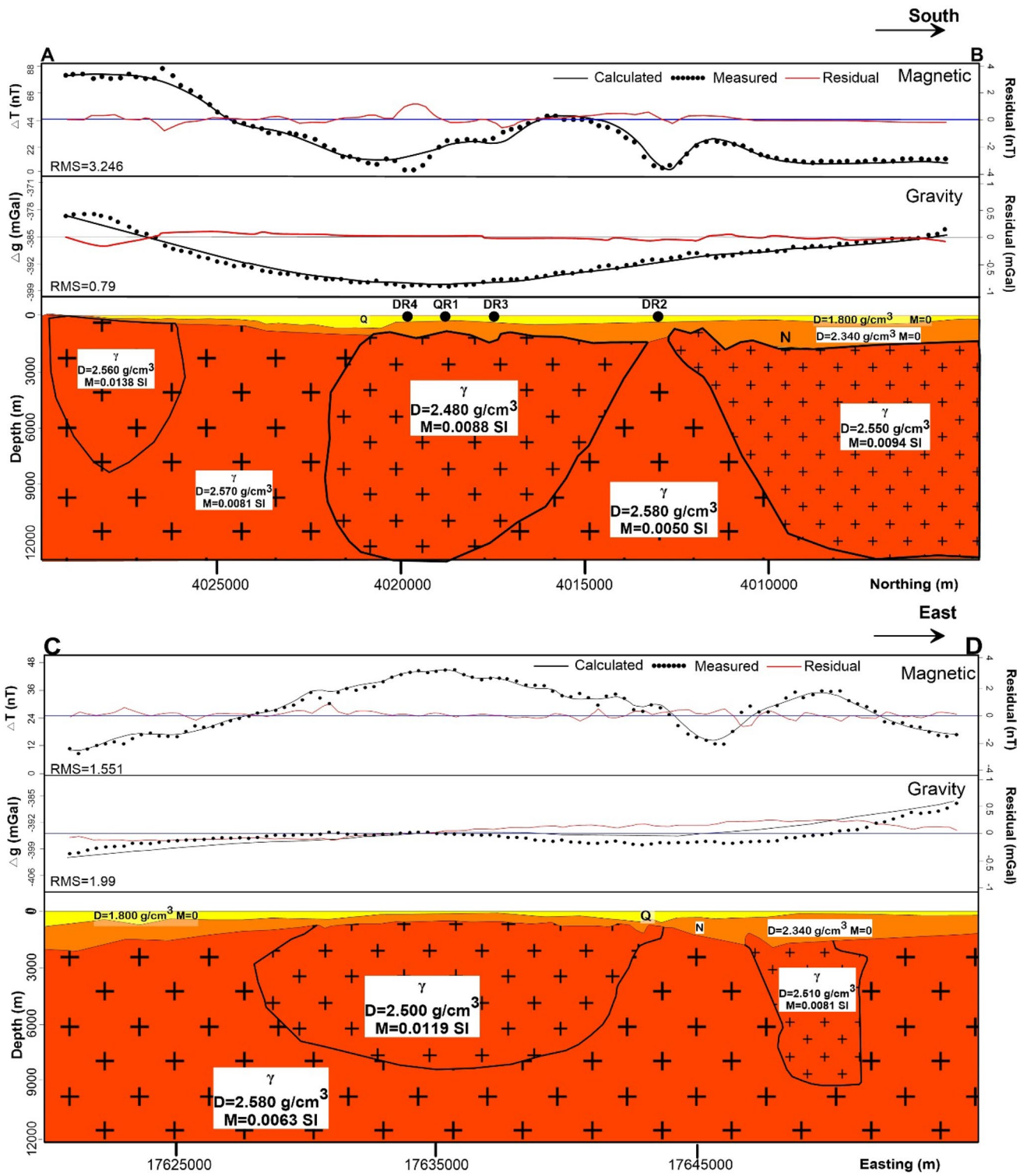


Fig. 3 2D manual joint inversion models of gravity and magnetic data in AB and CD profiles of the study area

changes, and two peaks appear, while the gravity one in this profile keeps stable at the rate of -394 mGal.

For both manual models, the density of the first and second layers are both estimated as 1.8 g/cm³ and 2.34 g/cm³, respectively. The susceptibility is assumed as zero, in terms of the contrast between the sediments and granites. The thickness of the sedimentary layers is then around 1500 m. Although the bases are composed of granites, they have different properties. In profile AB, there are five blocks. The density is set with a small change as 2.48 – 2.58 g/cm³. This is reasonable because there is no apparent gravity anomaly along the profile. The susceptibilities are in a range of 0.005 – 0.0138 SI. As for CD, there are three blocks. The major one is with a lower susceptibility (0.0063 SI) but a higher density (2.58 g/cm³). The other two blocks are in a smaller size and their bottom depth is around 8000 m. In addition, deep faults could be outlined between different blocks, which could reach to 12 km depth, as shown in AB.

3D joint inversion results

The inversed density and magnetic susceptibility models are depicted in Fig. 4. These models show the distribution of density and susceptibility deviation. The density deviation is to the 2.58 g/cm³, which is the assumed widespread granite density in the 2D manual inversion. For the magnetic susceptibility, it is the absolute value, when considering the susceptibility of the sedimentary layers is 0.

For these two models, they have different distributions and their own characteristics. For the density model in Fig. 4a, it could be divided into two parts in the vertical perspective. The upper zone (0 – 1400 m) is rather uniform in the low-value band (< -0.3 g/cm³). With the depth increases, the transition zone occurs at around 1400 – 2000 m. The density increases in the middle part. Below this area, the distribution of density goes to be stable and two blocks appear. One is in a higher density (> -0.1 g/cm³) and mainly locates in the north-eastern part covering Gonghe town and Dongba. The size of this block decreases little when it comes to 3000 – 3500 m. The other block with a low density (< -0.3 g/cm³) is in the south-western part, and its value is consistent when it goes deeper.

However, the susceptibility model in Fig. 4b has an entirely different trend. Its value ranges from 0 to 5×10^{-3} SI. In the top part within 0 – 600 m, it distributes dispersedly, and the value in the central part is relatively lower. Beneath this part, major block with the susceptibility of more than 3.5×10^{-3} SI exists in the central part of the area. The block is elongated in the NNE–SSW trend as in the kriged magnetic map. This block expands when it goes deeper and nearly covers the whole area at 3000 m depth. However, the block size decreases at the sections with 3000 m to about 3500 m depth.

Discussion

Several studies discuss the geothermal mechanism here. For the heat source, it might be the magma capsules or melted granites in the upper crust (Zhao et al. 2020). The instantaneous heat conductive process to transport the heat. (Wanamaker et al. 2004; Gao et al. 2018). From the resistivity models, there are several vertical narrow conductive zones between the near-surface conductive zone and the middle crust conductive zone as hidden faults. These faults are served as the channels for transporting heat from the heat source to the shallow zone (around the depth of 3000 m) (Gao et al. 2018). The difference of the density and susceptibility would be then affected by the melting bodies with the intrusion since Late Triassic (Zhang et al. 2018a).

When it goes to the shallow part, the 3D resistivity model from MT works shows significantly conductive anomalies at depths above ~ 3000 m, related to HDR or hydrothermal reservoirs. The Quaternary sediment layer serves as the cap for the geothermal system (Gao et al. 2018). The low-value anomaly in gravity data coincides with the location of the quaternary sedimentary deposits (Pan et al. 2009). It was formed after the basin uplift in Mesozoic (Fang et al. 2005). These layers have low permeability and can prevent heat from escaping. The sedimentary layers in the study area could be outlined in 1000 – 1500 m from our achieved models, but it is hard to point out the specific line between Quaternary and Neogene sedimentary rocks.

The strata distribution along the DR4–QR1–DR3–DR2 wells in Fig. 5a shows the hydrothermal and the HDR reservoirs from the Earth's surface to the 3300 m depth of the study area (Xu et al. 2018). The hydrothermal reservoirs are located at a depth of around 200 m and 700 – 1000 m. The granite rocks are in the deeper parts, but those with hot temperature (> 150 °C) are defined as HDR. For these wells, the temperature all increases sharply in Fig. 5b, with a gradient of around 40 – 50 °C/km. Notably, it reaches 150 °C at 2336 m depth for DR4, and 2104 m for DR3. The deep granite would be then defined as HDR.

Compared with the density and susceptibility models, there is consistency. The boundary between sedimentary layers and granite is located in somewhere between 900 and 1500 m depth. There is also a boundary between 0 and 1×10^{-3} SI, at nearly the same position in the susceptibility model, while the density model roughly matches for the boundary of -0.3 and -0.2 g/cm³. The water existing in sedimentary layers might reduce the density in a degree and cause the density mixture for the sedimentary parts. The boundary between non-HDR and HDR in 2200 – 2400 m fits the interface of -0.1 and 0 g/cm³ well, but there is not any susceptibility boundary at this level.

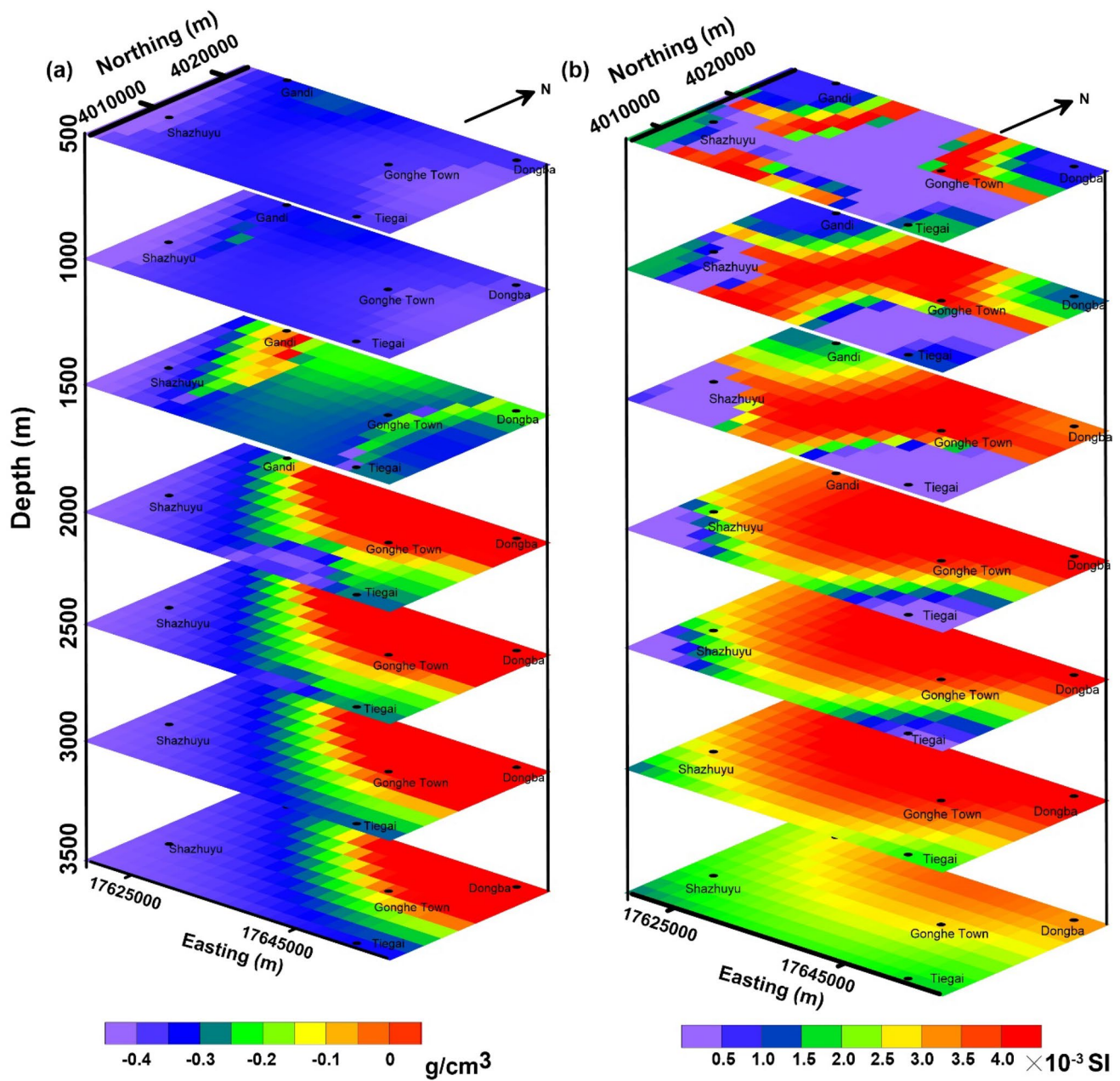


Fig. 4 Through 3D gravity and magnetic joint inversion: (a) 3D density model, (b) 3D magnetic susceptibility model

From these comparisons, the boundaries of HDR matches the density boundary between -0.2 and 0 g/cm^3 well, while the edge of the high susceptibility nearly fits the upper boundary of the granite. In this way, the density of HDR would be estimated over 2.6 g/cm^3 , and the density of sedimentary rocks on the ground is between 2.1 and 2.3 g/cm^3 . For the magnetic susceptibility, the HDR is estimated more than $4 \times 10^{-3} \text{ SI}$. By these standards, the prospective HDR districts are then circled at the area along Gonghe town and Dongba, and the volume would be then estimated as 6100 km^3 above 3500 m depth. Meanwhile, 2000 m would

be a preferable minimum depth for exploitation. With some pre-existing fractures, both 2D and 3D EGS modelling could be simulated along with the further engineering evaluation (MacFarlane et al. 2014; Xu et al. 2018).

For the HDR delineation here, temperature, stress and the hydrothermal alteration should be discussed for the change of density and susceptibility. Regardless of the minor change of mineral composition of granites, the porosity would be a major factor for the density change. However, the porosity decreases up to around $100 \text{ }^\circ\text{C}$ and then consecutively increase up to $800 \text{ }^\circ\text{C}$ (He et al. 2018).

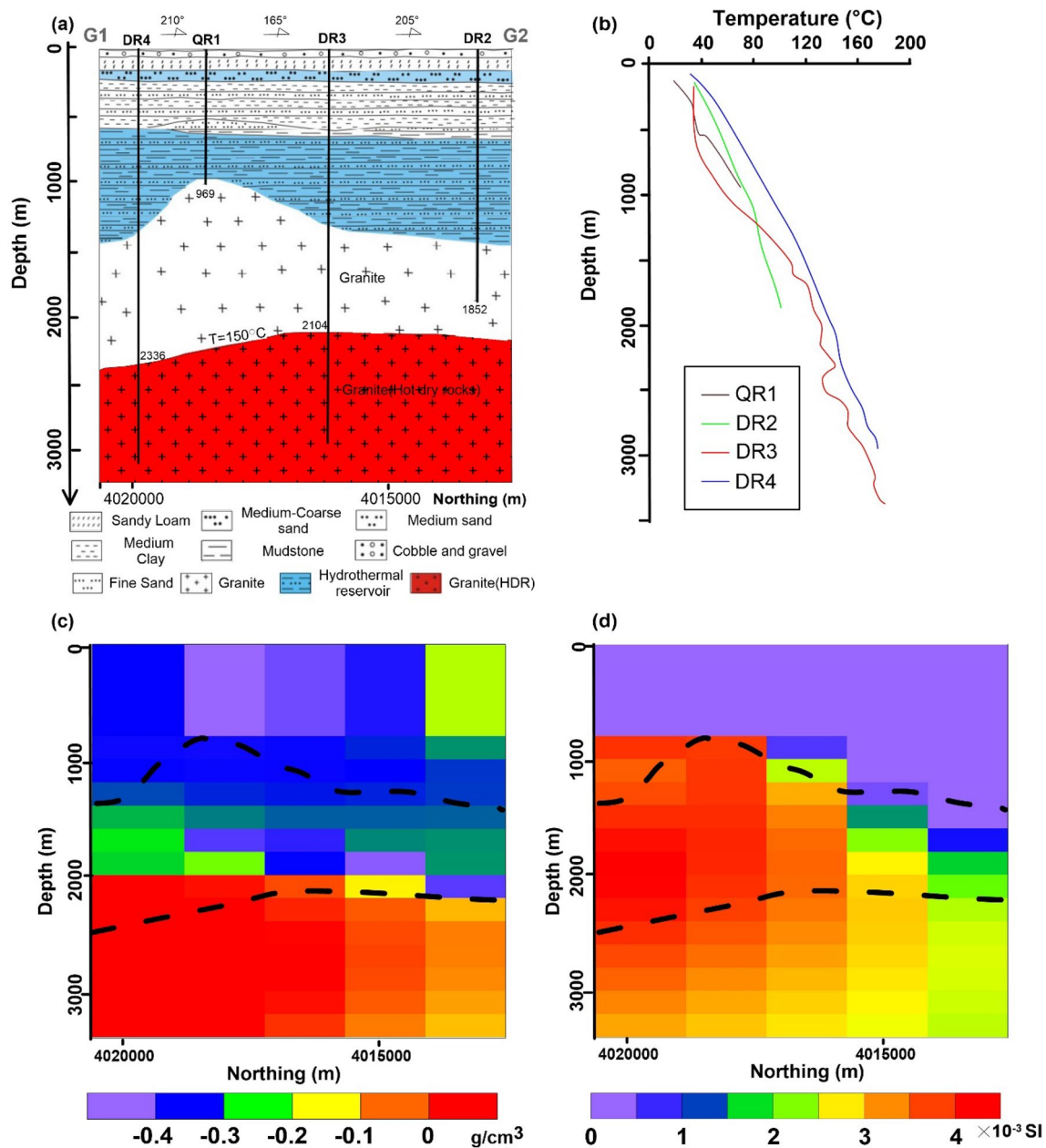


Fig. 5 The profile G1–G2 along DR2, DR3, DR4 and QR1 wells: (a) stratigraphic distribution based on drilling data (after Xu et al. 2018), (b) temperature logs of DR2, DR3, DR4 and QR1 (after Xu et al.

2018), (c) distribution of rock density based on the 3D density model, (d) distribution of magnetic susceptibility of the rocks according to the 3D magnetic susceptibility model

The temperature would not make the density increase. For the susceptibility, it changes slightly at 100–200 $^{\circ}\text{C}$ (Just and Kontny 2012). The overburden stress can cause the closure of microfractures and pore spaces, with an increased density of granite. At a depth of 2–3 km, the overburden stress in the study area is estimated at around 73–87 MPa (Weinert et al. 2020). Considering the effective stress in the sedimentary basin is generally lower than

20 MPa (e.g. Paul et al. 2010; Zhang 2013), the decreasing rate of porosity could reach around 2.5% (Jia et al. 2017). The hydrothermal alteration also affects the physical attribute here. Hou et al. (2019) used the integrated multicomponent geothermometry method to outline the conceptual model, with hot water flow in the fracture zone at the depth of around 2000 m. The alteration and weathering could then decrease the density of granite.

Conclusions

A gravity and magnetic survey was carried out in the Gonghe town in the potential Gonghe geothermal field. To better understand the areal and vertical distribution of the HDR, the gravity and magnetic data were inverted using 2D manual inversion and 3D cross-gradient joint inversion based on SLO-MS. The results indicate that this area is overlapped by the sedimentary layers, the thickness of which is around 1000–1500 m. Granites of different periods and intrusion processes are widely distributed and located under the sediments, with some deep faults.

As for the HDR delineation, it is mainly located along Gonghe town and Dongba. The density and susceptibility are inverted as over 2.6 g/cm^3 and $4 \times 10^{-3} \text{ SI}$, respectively. Its upper boundary is around 2000 m depth, and the volume is estimated as around 6100 km^3 in those parts whose depths are less than 3500 m.

The appearance of the density and magnetic susceptibility models are affected by the lithology, stress and hydrothermal alteration. Therefore, as for the EGS site location, reservoir temperature and structural patterns need more attention. At the heat exploitation stage, other geophysical methods including the microgravity, seismic and more detailed MT surveys (e.g. 4D inversion of time-lapse MT data sets) would be more applicable for monitoring the injected fluid (Nam et al. 2017). For the theoretical study, as the geothermal concept is still disputable in this area, regional gravity and magnetic data would be much beneficial for the regional structure delineation and geological modelling. For example, the long wave deviations in gravity and magnetic fields could also help to reveal the deep structures.

Acknowledgements The authors wish to thank reviewers for insightful suggestions, comments, and reviews and thoughtful comments. The authors also acknowledge all students working hard at the Gonghe area, regardless of extreme weather and the poor living condition. Financial supports for this research were provided by Key Research and Development Program of China (2020YFE0201300), Project [2016] 0707 of Centre for hydrogeology and environmental geology survey (China Geological Survey), National Natural Science Foundation of China (41874134) and the Excellent Youth Fund of Jilin Province (20190103142JH).

References

- Chen J, Jiang F (2015) Designing multi-well layout for enhanced geothermal system to better exploit hot dry rock geothermal energy. *Renew Energy* 74:37–48
- Dobrin MB, Savit CH (1960) Introduction to geophysical prospecting, vol 4. McGraw-hill, New York
- Fang B, Zhou X, Liang S (2009) Characteristics and utilization of the Zhacang hot springs in Guide County, Qinghai. *Geoscience* 23:57–63
- Fan B, Liu X, Zhu Q, Qin G, Li J, Lin H, Guo L (2020) Exploring the interplay between infiltration dynamics and critical zone structures with multiscale geophysical imaging: a review. *Geoderma* 374:114431
- Fang X, Yan M, Van der Voo R, Rea DK, Song C, Parés JM, Gao J, Nie J, Dai S (2005) Late Cenozoic deformation and uplift of the NE Tibetan Plateau: evidence from high-resolution magnetostratigraphy of the Guide Basin, Qinghai Province, China. *Geol Soc Am Bull* 117:1208–1225
- Gabtni H, Jallouli C (2017) Regional-residual separation of potential field: an example from Tunisia. *J Appl Geophys* 137:8–24
- Gallardo LA, Meju MA (2004) Joint two-dimensional DC resistivity and seismic travel time inversion with cross-gradients constraints. *J Geophys Res Sol Earth* 109.
- Gallardo LA, Meju MA (2011) Structure-coupled multiphysics imaging in geophysical sciences. *Revi Geophys* 49.
- Gao J, Zhang H, Zhang S, Chen X, Cheng Z, Jia X, Li S, Fu L, Gao L, Xin H (2018) Three-dimensional magnetotelluric imaging of the geothermal system beneath the Gonghe Basin, Northeast Tibetan Plateau. *Geothermics* 76:15–25
- Guiling W, Yanguang L, Xi Z, Wei Z (2020) The status and development trend of geothermal resources in China. *Earth Sci Front* 27(1):001–009
- He L, Yin Q, Jing H (2018) Laboratory investigation of granite permeability after high-temperature exposure. *Processes* 6:36
- He R, Zeng Z, Zhao X, Du W, Huo Z, Song E (2017) Interpretation of gravity data to delineate underground structure in the Gonghe geothermal field, China. International Geophysical Conference, Qingdao, China, 17–20 April 2017. Society of Exploration Geophysicists and Chinese Petroleum Society. pp 863–866
- Hou Z, Xu T, Li S, Jiang Z, Feng B, Cao Y, Feng G, Yuan Y, Hu Z (2019) Reconstruction of different original water chemical compositions and estimation of reservoir temperature from mixed geothermal water using the method of integrated multicomponent geothermometry: a case study of the Gonghe Basin, northeastern Tibetan Plateau, China. *Appl Geochem* 108:104389
- Hu N (1991) Physical features of regional rock in Qinghai province. *Qinghai Geol* 1:42–52
- Jacobsen BH (1987) A case for upward continuation as a standard separation filter for potential-field maps. *Geophysics* 52:1138–1148
- Jarvis A, Reuter HI, Nelson A, Guevara E (2008) Hole-filled SRTM for the globe Version 4. CGIAR-CSI SRTM 90m Database (<https://srtm.csi.cgiar.org>) 15:25–54.
- Jelacic A, Fortuna R, LaSala R, Nathwani J, Nix G, Visser C, Green B, Renner J, Blankenship D, Kennedy M (2008) An Evaluation of Enhanced Geothermal Systems Technology. Office of Energy Efficiency and Renewable Energy (EERE), Washington, DC
- Jia C, Xu W, Wang H, Wang R, Yu J, Yan L (2017) Stress dependent permeability and porosity of low-permeability rock. *J Cent South Univ* 24:2396–2405
- Just J, Kontny A (2012) Thermally induced alterations of minerals during measurements of the temperature dependence of magnetic susceptibility: a case study from the hydrothermally altered Soultz-sous-Forêts granite, France. *Int J Earth Sci* 101:819–839
- Kana JD, Djongyang N, Raidandi D, Nouck PN, Dadjé A (2015) A review of geophysical methods for geothermal exploration. *Renew Sustain Energy Rev* 44:87–95
- Khair HA, Cooke D, Hand M (2015) Seismic mapping and geometrical analyses of faults within deep hot granites, a workflow for enhanced geothermal system projects. *Geothermics* 53:46–56
- Li X, Main I, Jupe A (2018) Induced seismicity at the UK ‘hot dry rock’ test site for geothermal energy production. *Geophys J Int* 214:331–344
- Liu M, Guo Q, Zhang C, Zhu M, Li J (2017) Sulfur isotope geochemistry indicating the source of dissolved sulfate in Gonghe

- geothermal waters, northwestern China. *Proc Earth Planet Sci* 17:157–160
- Lu C, Lin W, Gan H, Liu F, Wang G (2017) Occurrence types and genesis models of hot dry rock resources in China. *Environ Earth Sci* 76:646
- MacFarlane J, Thiel S, Pek J, Peacock J, Heinson G (2014) Characterisation of induced fracture networks within an enhanced geothermal system using anisotropic electromagnetic modelling. *J Volcanol Geotherm Res* 288:1–7
- Maxwell S (2014) Microseismic imaging of hydraulic fracturing: Improved engineering of unconventional shale reservoirs. *Society of Exploration Geophysicists*
- Nabighian MN, Grauch V, Hansen R, LaFehr T, Li Y, Peirce J, Phillips J, Ruder M (2005) The historical development of the magnetic method in exploration. *Geophysics* 70:33ND–61ND
- Nam MJ, Song Y, Jang H, Kim B (2017) 4D inversion of time-lapse magnetotelluric data sets for monitoring geothermal reservoir. *J Appl Geophys* 141:88–97
- Oasis-Montaj (2006) Gravity and magnetic software, user manual. Oasis Montaj 6.
- Over S, Akin U, Sen R (2018) Geophysical data (gravity and magnetic) from the area between Adana, Kahramanmaraş and Hatay in the eastern mediterranean region: tectonic implications. *Pure Appl Geophys* 175:2205–2219
- Pak Y, Li T, Kim G (2017) 2D data-space cross-gradient joint inversion of MT, gravity and magnetic data. *J Appl Geophys* 143:212–222
- Pan G, Xiao Q, Lu S, Deng J, Feng Y, Zhang K, Zhang Z, Wang F, Xing G, Hao G-J (2009) Subdivision of tectonic units in China. *Geol China* 36:1–28
- Panel M-II (2006) The future of geothermal energy: impact of enhanced geothermal systems (EGS) on the United States in the 21st century. *Geothermics* 17:881–882
- Paul S, Chatterjee R, Kundan A (2010) Determination of In-situ Stress Magnitudes for an Offshore Basin of Eastern India. 8th Biennial International Conference and Exposition on Petroleum Geophysics, Hyderabad, India, 1st–3rd Feb.
- Peacock JR, Thiel S, Reid P, Heinson G (2012) Magnetotelluric monitoring of a fluid injection: example from an enhanced geothermal system. *Geophysical Research Letters* 39.
- Pollack HN, Hurter SJ, Johnson JR (1993) Heat flow from the earth's interior: analysis of the global data set. *Rev Geophys* 31:267–280
- Portniaguine O, Zhdanov MS (2002) 3-D magnetic inversion with data compression and image focusing. *Geophysics* 67:1532–1541
- Represas P, Santos FM, Ribeiro J, Ribeiro JA, Almeida EP, Gonçalves R, Moreira M, Mendes-Victor L (2013) Interpretation of gravity data to delineate structural features connected to low-temperature geothermal resources at Northeastern Portugal. *J Appl Geophys* 92:30–38
- Reudink R, Klees R, Francis O, Kusche J, Schlesinger R, Shabanloui A, Sneeuw N, Timmen L (2014) High tilt susceptibility of the Scintrex CG-5 relative gravimeters. *J Geodesy* 88:617–622
- Samrock F, Kuvshinov A, Bakker J, Jackson A, Fisseha S (2015) 3-D analysis and interpretation of magnetotelluric data from the Aluto-Langano geothermal field, Ethiopia. *Geophys J Int* 202:1923–1948
- Sun Y, Fang H, Zhang K, Zhao F, Liu S (2007) Step-like landform system of the Gonghe basin and the uplift of the Qinghai–Tibet Plateau and development of the Yellow River. *Geol China* 34:1141–1147
- Sun Z, Li B, Wang Z (2011) Exploration of the possibility of hot dry rock occurring in the Qinghai Gonghe Basin. *Hydrogeol Eng Geol* 38:119–124
- Tóth G, Ádám J, Földváry L, Tziavos IN, Denker H (2005) Calibration/validation of GOCE data by terrestrial torsion balance observations. In: Sansó F (ed) *A window on the future of geodesy, IAG Symposium, vol 128*. Springer, Berlin, pp 214–219
- Uwidiuhaye JdA, Mizunaga H, Saibi H (2018) Geophysical investigation using gravity data in Kinigi geothermal field, northwest Rwanda. *J Afr Earth Sc* 139:184–192
- Wang B (2006) 2D and 3D potential-field upward continuation using splines. *Geophys Prospect* 54:199–209
- Wang J, Hu S, Pang Z, He L, Zhao P, Zhu C, Rao S, Tang X, Kong Y, Luo L (2012) Estimate of geothermal resources potential for hot dry rock in the continental area of China. *Sci Technol Rev* 30:32
- Wannamaker PE, Rose PE, Doerner WM, Berard BC, McCulloch J, Nurse K (2004) Magnetotelluric surveying and monitoring at the Coso geothermal area, California, in support of the enhanced geothermal systems concept: survey parameters and initial results. *Proceedings of the Twenty-Ninth Workshop on Geothermal Reservoir Engineering, Stanford University*. pp 287–294
- Weinert S, Bär K, Sass I (2020) Thermophysical rock properties of the crystalline Gonghe Basin Complex (Northeastern Qinghai–Tibet Plateau, China) basement rocks. *Environ Earth Sci* 79:77
- Xi Y, Wang G, Liu S, Zhao Y, Hu X (2018) The formation of a geothermal anomaly and extensional structures in Guangdong, China: evidence from gravity analyses. *Geothermics* 72:225–231
- Xie L, Min K-B (2016) Initiation and propagation of fracture shearing during hydraulic stimulation in enhanced geothermal system. *Geothermics* 59:107–120
- Xing C (2017) Gravity and magnetic data processing in Qiabuqia. Jilin University, Qinghai
- Xu T, Liang X, Feng B, Jiang Z (2019) Geologic Setting of the Potential EGS Site at the Gonghe Basin, China: Suitability for Research and Demonstration of Hot Dry Rock Geothermal Energy Development. 44th Workshop on Geothermal Reservoir Engineering, Stanford University
- Xu T, Yuan Y, Jia X, Lei Y, Li S, Feng B, Hou Z, Jiang Z (2018) Prospects of power generation from an enhanced geothermal system by water circulation through two horizontal wells: a case study in the Gonghe Basin, Qinghai Province, China. *Energy* 148:196–207
- Yan W (2015) Characteristics of Gonghe Basin hot dry rock and its utilization prospects. *Sci Technol Rev* 33:54–57
- Yue G, Deng X, Xing L, Lin W, Liu F, Liu Y, Wang G (2015) Numerical simulation of hot dry rock exploitation using enhanced geothermal systems in Gonghe Basin. *Sci Tech Rev* 33:62–67
- Zaher MA, Saibi H, Mansour K, Khalil A, Soliman M (2018) Geothermal exploration using airborne gravity and magnetic data at Siwa Oasis, Western Desert, Egypt. *Renew Sustain Energy Rev* 82:3824–3832
- Zarrouk SJ, Moon H (2014) Efficiency of geothermal power plants: a worldwide review. *Geothermics* 51:142–153
- Zeng H, Xu D, Tan H (2007) A model study for estimating optimum upward-continuation height for gravity separation with application to a Bouguer gravity anomaly over a mineral deposit, Jilin province, northeast China. *Geophysics* 72:145–150
- Zhang C, Jiang G, Shi Y, Wang Z, Wang Y, Li S, Jia X, Hu S (2018a) Terrestrial heat flow and crustal thermal structure of the Gonghe-Guide area, northeastern Qinghai–Tibetan plateau. *Geothermics* 72:182–192
- Zhang G, Guo A, Yao A (2004) Western Qinling–Songpan continental tectonic node in China's continental tectonics. *Earth Sci Front* 3.
- Zhang H, Chen Y, Xu W, Liu R, Yuan H, Liu X (2006) Granitoids around Gonghe basin in Qinghai province: petrogenesis and tectonic implications. *Acta Petrologica Sinica* 22:2910–2922
- Zhang J (2013) Effective stress, porosity, velocity and abnormal pore pressure prediction accounting for compaction disequilibrium and unloading. *Mar Pet Geol* 45:2–11
- Zhang J, Zeng Z, Zhao X, Li J, Zhou Y, Gong M (2020) Deep mineral exploration of the Jinchuan Cu–Ni sulfide deposit based on aeromagnetic, gravity, and CSAMT methods. *Minerals* 10:168
- Zhang S, Yan W, Li D, Jia X, Zhang S, Li S, Fu L, Wu H, Zeng Z, Li Z (2018b) Characteristics of geothermal geology of the

Qiabuqia HDR in Gonghe Basin, Qinghai Province. *Geol China* 45:1087–1102

Zhao X, Zeng Z, Huai N, Wang K (2020) Geophysical responses and possible geothermal mechanism in the Gonghe Basin, China. *Geomech Geophys GeoEnergy GeoResour* 6:1–12

Zhao X, Zeng Z, Zhang Q, Chen X (2019) The implication of the geophysical data and drilling records for the formation and paleoenvironment of the Hobq Desert, China. *Quatern Int* 519:42–49

Publisher's Note Springer Nature remains neutral with regard to jurisdictional claims in published maps and institutional affiliations.